Open Ceramics 6 (2021) 100111

Contents lists available at ScienceDirect

Open Ceramics

journal homepage: www.editorialmanager.com/oceram

Direct comparison of multi and single-phase models depicting the drying process of refractory castables

M.H. Moreira [a,b,*], S. Dal Pont [d], R.F. Ausas [c], T.M. Cunha [a,b], A.P. Luz [a,b], V.C. Pandolfelli [a,b]

[a] Federal University of Sao Carlos, Graduate Program in Materials Science and Engineering (PPGCEM), Rod. Washington Luiz, Km 235, 13565-905, São Carlos, SP, Brazil
[b] Federal University of Sao Carlos, Materials Microstructural Engineering Group (FIRE Associate Laboratory), Rod. Washington Luiz, Km 235, 13565-905, São Carlos, SP, Brazil
[c] Institute of Mathematics and Computer Sciences, University of São Paulo, São Carlos, SP, 13566-590, Brazil
[d] CNRS, Grenoble INP, 3SR, Université Grenoble Alpes, 38000, Grenoble, France

ARTICLE INFO

Keywords:
Refractory
Drying
Simulation
Multi-phase
Single-phase

ABSTRACT

Refractory castables are crucial for the production of steel and other materials. Upon heating, pressurization of vapor within their pores is developed, which may lead to cracks and even explosions. Numerical simulations are valuable tools for studying and developing strategies to prevent such phenomena during the drying stage. These mathematical models are categorized as single-phase or multiphase depending on whether the moving phases are considered individually or represented by a single entity. In this paper, an unprecedented direct comparison of such approaches is presented pointing out that the single-phase models could represent the experimental results to a reasonable extent with some minor caveats. To fulfill this task the modelling results were compared with those obtained by pressure and temperature measurements and using neutron tomography tests. Particularly, the multiphase model that considered the effect of capillary pressure could predict specific aspects such as the water accumulation ahead of the drying front.

1. Introduction

Refractory castables define a specific category of monolithic material that is directly shaped when applied [1,2]. As the development of chemical bonding among the components of such ceramic products will only be formed after sintering at high temperatures, a binder system that provides their green mechanical strength is required. The most common option is the class of hydraulic binders, which is based on chemical compounds that develop strength due to hydration reactions. The major representative is the calcium aluminate cement, which precipitates hydrated phases containing different stoichiometry of CaO and Al_2O_3 after its interaction with water during the castables' processing steps [2].

Although monolithics have numerous advantages over shaped products, such as easier application, no need for numerous joints (which are likely sites for corrosion initiation), and the possibility of automation of its application, some special attention is still required during the initial steps of their drying. This is a consequence of the risk of explosive spalling [2], which is related to the thermomechanical stresses and the pore pressurization of water vapor originated from dehydration and evaporation of reminiscent unreacted and reacted water [3].

This phenomena can also be seen when structures made of Portland cement concretes are on fire [4]. Portland cement strength also derives from the precipitation of hydrated phases, however, instead of containing CaO and Al_2O_3, this binder is mainly comprised of CaO and SiO_2 [5]. Given the importance of this structural material for civil constructions such as tunnels, buildings and nuclear reactor walls, fire safety concerns led to the development of various studies [4,6–11].

Indeed, it was within the scope of Portland cement concrete structures under intense heating that the first numerical models were developed [6], according to the mathematical model based on classical irreversible thermodynamics proposed by Luikov [12], Bažant also considered the concrete microstructure, proposing a single-phase model in which the fluid phase was controlled by the movement of the hindered adsorbed water among the solid particles [6,13,14].

Bažant also developed semi-empirical relationships of concrete properties, such as the sorption isotherms that describe the amount of evaporable water inside the concrete, permeability, and dehydration water release. The model provided the possibility of attaining relative humidity higher than 100%, which has a debatable physical meaning.

* Corresponding author. Federal University of Sao Carlos, Graduate Program in Materials Science and Engineering (PPGCEM), Rod. Washington Luiz, km 235, 13565-905, São Carlos, SP, Brazil.
E-mail address: murilo.moreira@estudante.ufscar.br (M.H. Moreira).

https://doi.org/10.1016/j.oceram.2021.100111
Received 24 February 2021; Received in revised form 21 April 2021; Accepted 22 April 2021
Available online 1 May 2021

Nomenclature

$(\overline{\rho C_p})$	effective heat capacity of concrete [J/(m^3 K)]
$\overline{\rho}_i$	mass of phase i per unit volume of concrete [kg/m^3]
ΔH_s	enthalpy of vaporization of water [J/kg]
Δm_{dehyd}	mass released by dehydration [kg/m^3]
δ_i	parameter that defines the central difference approximation
ε	emissivity [−]
ε_i	volume fraction of phase i [−]
$\widehat{w}_{change}$	normalized relative water change at a specific moment [−]
κ	hydraulic conductivity [m/s]
λ	thermal conductivity [W/(m K)]
$\hat{\mathbf{n}}$	normal unit vector
μ_i	Dynamic viscosity of phase i [Pa s]
$\overline{\rho C_p \vec{v}}$	vector of energy transport by fluid flow [J/(m^2 K)
φ	porosity [−]
ρ_i	density of phase i [kg/m^3]
σ	Stefan-Boltzmann's constant [5.67 10^{-8} W/(m^2 K^4)]
$\widetilde{(\cdot)}$	variable defined per unit volume of gaseous mixture
$\vec{J}_i$	Mass flux density of phase i [kg/(m^2 s)]
$C_{p,i}$	isobaric specific heat of phase i [J/(kg K)]
D_b	diffusivity of adsorbed water [m^2/s]
D_{AV}	diffusion coefficient of air or vapor in the gaseous mixture [m^2/s]
g	acceleration of gravity [m/s^2]
h_i	mass transfer coefficient of phase i [s/m]
h_m	mass transfer coefficient [s/m]
h_T	heat transfer coefficient [W/m^{2}K]
K_0	initial intrinsic permeability [m^2]
K_g	relative permeability of the gas phase [−]
K_k	Klinkenberg correction factor [−]
K_l	relative permeability of the liquid phase [−]
p_i	pressure of phase i [N/m^2]
S_b	pore saturation with adsorbed water [−]
S_l	pore saturation with liquid [−]
S_{ssp}	solid saturation point [−]
T	temperature [K]
t	time [s]
w_i	initial water content [kg/m^3]
w_{change}	relative water change at a specific moment [kg/m^3]

Subscript

d	chemically bound water
e	evaporable water
env	property of the environment
l	liquid water

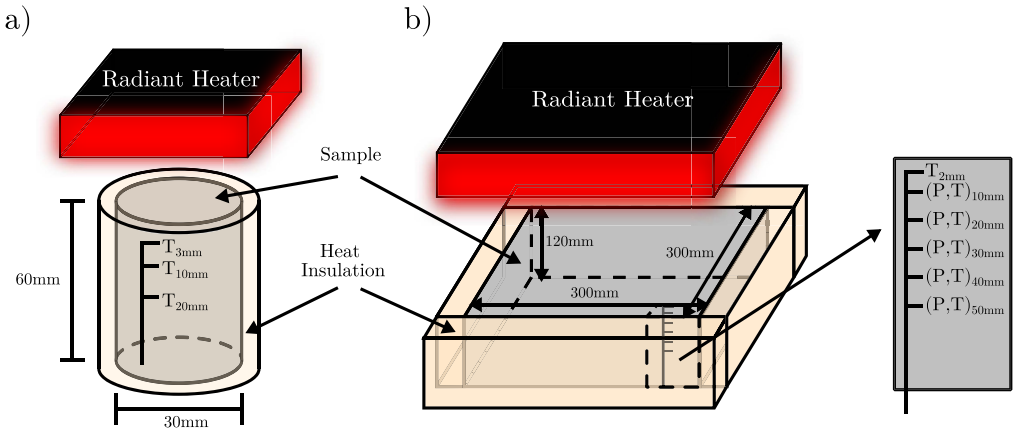

Fig. 1. Overview of the experimental setup used for (a) the neutron tomography tests and (b) the PTM ones used as reference for the numerical models.

Although this point was considered as one major drawback of this model [11,15], Bažant justifies that such a scenario is possible when one considers an anticlastic meniscus with negative curvature radius [14]. Despite its simplicity (and probably also because of it), Bažant's model is one of the most common methodologies applied to simulate concrete exposed to fire [15]. Gong et al. [16,17] and Palmer et al. [18] also used this approach to study the drying of refractory castables. Recently, new developments based on Bažant's work yield mesoscale modelling of refractory castables and polymeric fibers providing new tools for studying and designing additives to decrease the probability of explosive spalling [19].

Meanwhile, another modelling approach was developed, where conversely the flow of each fluid phase was considered separately. The main representative of this class of models is the one proposed by Gawin et al. [20], which also considers the thermomechanical behavior of concrete, and the kinetic models of chemical and mechanical damage. A detailed thermodynamic analysis of Gawin's model, points out that its selection of primary variables and its main hypothesis are consistent [21], making it one of the most physically accurate models to account for the different phenomena involved in drying.

It should be noted that one of the main criticisms of this model is that the porosity of concrete is not totally interconnected and, therefore, an approach that considers the flow of each phase individually might not be accurate [14]. Another drawback of this model is that they demand numerous input parameters and rely on properties that are not easily measured, which inhibits its technological application, specially when comparing numerous materials with distinct properties.

Although different approaches were proposed [14,22] recently, the homogenized continuum multi and single-phase treatment of the problem remains the most popular tool to describe the drying behavior of concrete and refractories castables at high temperatures [23–25].

Considering specifically the refractories, Fey et al. [23,26,27] applied a multiphase model that neglected the effect of capillary pressure based on the works by Tenchev and Davie [28,29] to study, i) the effect of

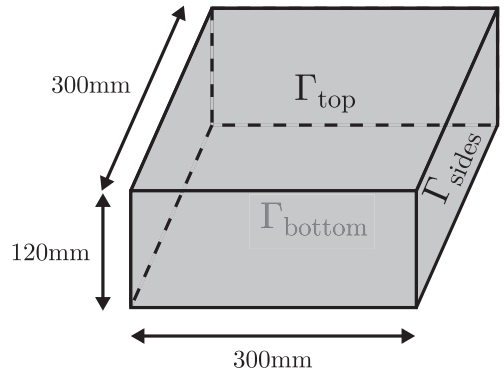

Mass Boundary Conditions	Thermal Boundary Conditions
Permeable on Γ_{top}	Heating by thermal radiation and natural convection on Γ_{top}
Permeable on Γ_{sides}	Adiabatic on Γ_{sides}
Impermeable on Γ_{bottom}	Cooling by natural convection on Γ_{bottom}

Fig. 2. Geometry and boundary conditions of the modelling of the PTM test.

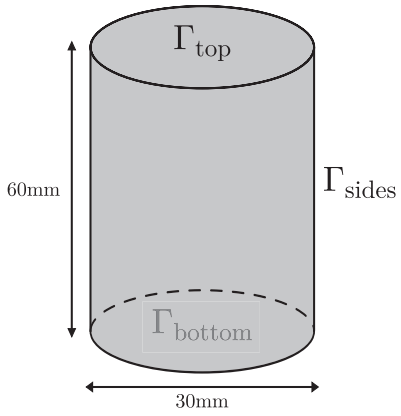

Mass Boundary Conditions	Thermal Boundary Conditions
Permeable on Γ_{top}	Heating by thermal radiation and natural convection on Γ_{top}
Permeable on Γ_{sides}	Adiabatic on Γ_{sides}
Impermeable on Γ_{bottom}	Cooling by natural convection on Γ_{bottom}

Fig. 3. Geometry and boundary conditions of the modelling of the neutron tomography test.

properties on the predicted maximum pressures, ii) the inclusion of a proportional integral derivative (PID) controller to design safe heating procedures and, iii) the effect of multiple layers of distinct materials. No clear explanation on why this specific model was adopted by the authors neither comparisons with simplified models were provided in that study.

To the best of the authors' knowledge, no direct comparison of such methods is available in the literature, neither for refractory castable nor for structural Portland cement concrete. Gawin et al. provided an interesting review that focused on assessing the importance of the different aspects of their model [15,20]. These authors analyzed the effect of neglecting specific properties on their model without directly comparing it with the other ones in the literature.

Therefore, the current work aims to fulfill this gap by comparing the single and multiphase approaches evaluating the predictive capacity of each model via reference experimental results of temperature and pressure (this setup is also known as PTM) [30], as well as neutron tomography studies [31–33]. The latter experimental results present the advantage of yielding 3D scans that describe the moisture distribution within the sample. All models considered in this study were implemented using the open source finite element framework FEniCS [34]. Validation of the implemented models was carried out by comparing the results with those published by the different authors.

Once the models have been validated, by yielding similar results to the ones present in the original works, they were used to simulate the experimental tests. The objective of this work was to provide an unprecedented comparison which may guide researchers to further develop their models and also help end-users to choose the appropriate ones considering the balance among theoretical fidelity, the various mechanisms involved in the physical process and the easiness of the numerical implementation.

2. Materials and methods

The current section presents the experimental techniques that were used as reference and the three different models that were selected for testing. For each model, a short review of the main assumptions and the balance equations are shown. The last section aims to describe the setup case. The materials considered in the analysis and their properties are presented in Appendix A.

2.1. Pressure and temperature measurements, and neutron tomography tests

The most common experimental technique for assessing the behavior of concrete (and refractory castable) at high temperatures is the PTM test [11,23,33], where pressure transducers and thermocouples are placed at different depths of a sample to record such properties during a one-directional heating test. The mass evolution of the sample can also be assessed (hence the acronym PTM). This test provides the evolution of temperature and pressure at specific positions, which can be compared to the results obtained by numerical simulations. As the input parameters of the different models are challenging to be measured at such extreme conditions, some properties of concrete are usually adjusted to match the results of the PTM test [9,23,35].

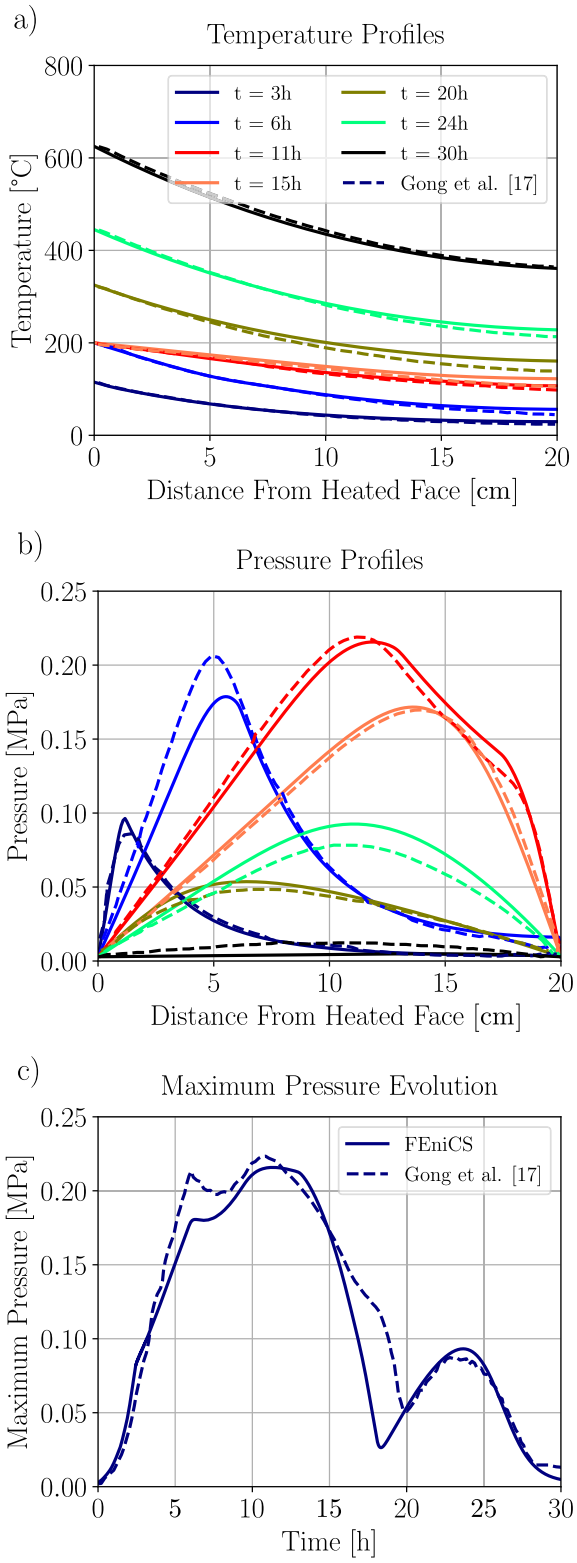

Fig. 4. Validation of the single-phase model. For the original results, see Ref. [17].

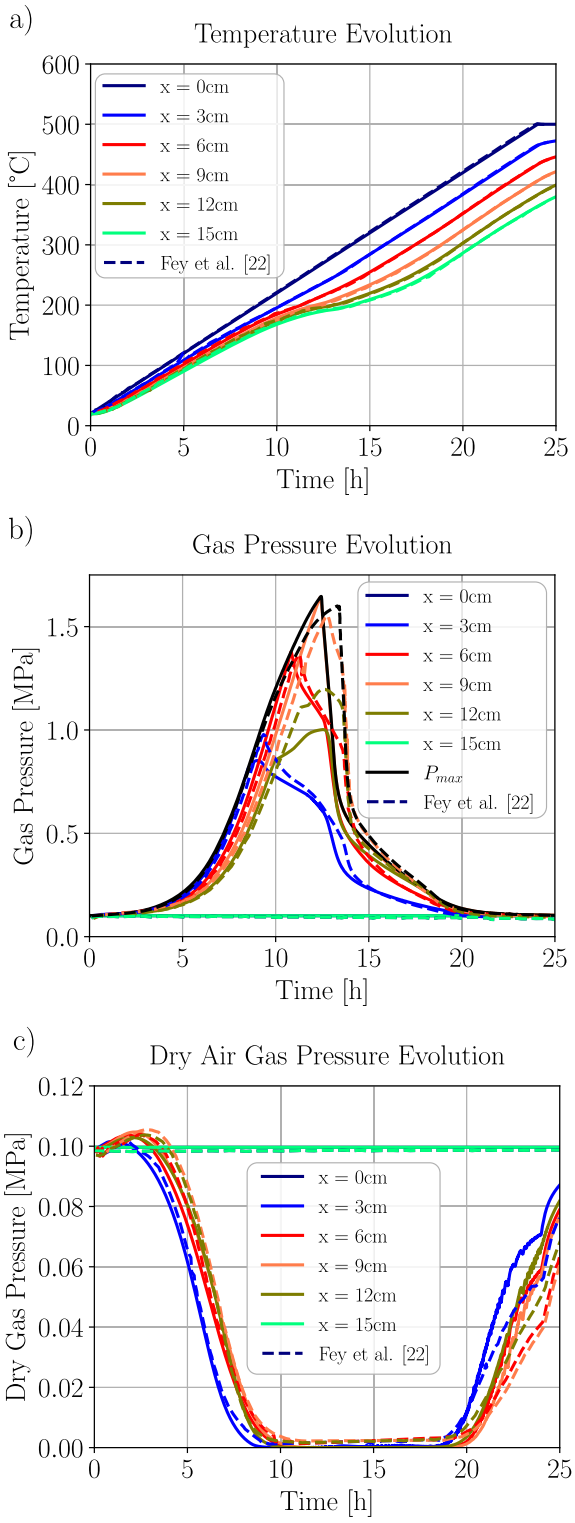

Fig. 5. Validation of the multiphase neglecting capillary effects model. For the original results, see Ref. [23].

Although this methodology is of great interest to provide important insights, there are fundamental issues related to this technique. The most important is that the thermomechanical properties of the sensors and concrete are different, yielding thermal stresses upon heating, which could generate microcracks around the sensors, directly affecting the local permeability and the observed behavior [23,33]. Another problem is that air bubbles can be formed on the surface of the sensors when the samples are cast, giving rise to defects that also influence the local properties. Interestingly, this situation was observed even using thermocouples as thin as 0.25 mm in diameter [33].

Thus, experimental techniques that do not rely on sensors placed within the samples can be of great interest. Recently, tomography studies have been proposed [31–33,36,37], based on the interaction of X-ray or

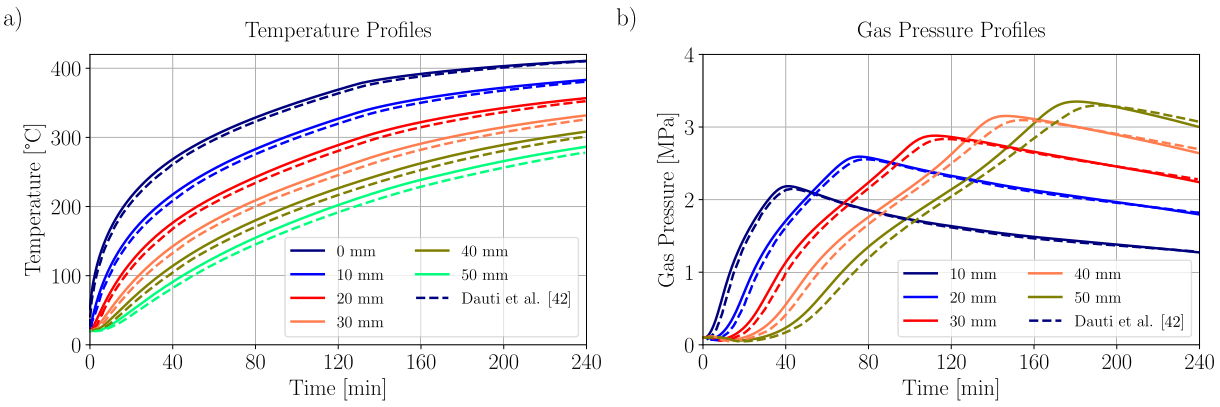

Fig. 6. Validation of the multiphase model considering capillary effects. For the original results, see Refs. [43,44].

neutrons with the microstructure of partially saturated concrete. The neutron tomography has the advantage of strongly interacting with the hydrogen nuclei in the water molecules. Moreover, the aggregates have a lower absorption which make it possible to distinguish the drying front inside the sample with no effect of the measurement methodology.

One major drawback of this technique is the limited size of the samples that can be used, as even materials that can be considered transparent to the neutron flux absorb a fraction of it, and, end up behaving as an opaque one. For the sake of comparison, the dimensions of the cylinder samples are 30 mm in diameter and 60 mm high, whereas the samples used for the PTM tests are slabs of 300 mm × 300 mm x 120 mm (see Fig. 1).

In the current work, neutron tomography tests carried out at the NeXT tomograph [38] at the Institute Laue-Langevin (ILL) will be used as the reference data to be compared with the numerical models. This equipment provides the world's highest cold neutron flux available for imaging samples. As a complete tomography can be obtained in a single minute, using such temporal resolution enables the analysis of the phenomena in real time.

After acquiring the tomographies, the images are processed in order to reconstruct the 3D geometry. At this step, various procedures are applied to correct likely sources of noise, such as the beam hardening effect, which is a spurious reduction of the gray value in the bulk of the sample.

A threshold filter is used to disregard the aggregates and the other bodies surrounding the sample, as the attention is upon the water transport within the cement paste. As this mask is applied, analysis of the moisture profile (which is the distribution of the normalized gray value through the sample, indicating the attenuation due to the hydrogen absorption of neutrons) or the drying rate (the ratio between the dry cement at a specific instant and the initial value) [31] can be obtained.

A sketch of the experimental methodology is shown in Fig. 1 (a). For further details, the reader can be referred to the works by Dauti et al. [31,33]. The PTM test is also represented in Fig. 1 (b).

2.2. Single-phase model

Based on the analysis of the pore structure of concrete [13,14], Bažant et al. proposed that the mass transfer within the material is limited by the transport of adsorbed water [6]. Thus, considering that the movement of separated phases could be seen as an unnecessary complication and that the mass balance equation could be written considering the flow of moisture, that is, the sum of the vapor and liquid water phases. The balance equations can be found in Equations (1) and (2). The nomenclature used for these equations is presented in the list available at the beginning of this work.

$$\frac{\partial \overline{\rho}_e}{\partial t} = \nabla \cdot \left(\frac{\kappa}{g} \nabla p_v \right) + \frac{\partial \overline{\rho}_d}{\partial t} \tag{1}$$

$$\rho_{eff} C_{p,eff} \frac{\partial T}{\partial t} = \nabla \cdot \left(\lambda_{eff} \nabla T \right) - C_{p,l} \frac{\kappa}{g} \nabla p_v \cdot \nabla T + \Delta H_{vap} \frac{\partial w}{\partial t} \tag{2}$$

The thermal boundary conditions that may be considered are the imposition of specific temperatures through Dirichlet type ones, or the definition of convection heat transfer on the surface by means of Newton's cooling law, or the use of radiant heat transfer. These take the form of Equations (3) and (4).

$$-\hat{\mathbf{n}} \cdot \lambda_{eff} \nabla T = h_T (T - T_\infty) \tag{3}$$

$$-\hat{\mathbf{n}} \cdot \lambda_{eff} \nabla T = \sigma \varepsilon \left(T^4 - T_\infty^4 \right) \tag{4}$$

Meanwhile, the conditions regarding the mass transport are based on the definition of mass flux by the difference of partial pressure of vapor between the ambient and the surface of the domain. This is achieved via a relationship similar to Newton's law of cooling based on the Chilton-Colburn analogy [28], as seen in Equation (5).

$$-\hat{\mathbf{n}} \cdot \frac{\kappa}{g} \nabla p_v = h_m (P_v - P_{v,\infty}) \tag{5}$$

Finally, adiabatic or impermeable scenarios for heat and mass transfer, respectively, can be achieved by defining a zero Neumann boundary condition, which naturally emerges in the variational formulation of the problem to be used for discretization [39].

2.3. Multiphase model neglecting capillary effects

The model described by Fey et al. [23] is an example of a multiphasic model with intermediate complexity. It is based on the works by Tenchev and Davie [28,29], and it considers the adsorbed water flux but it neglects the effect of the capillary pressure (thus, referenced as the multiphase model neglecting capillary effects, MP-NCP). The primary variables are: the temperature, the dry air pressure and the vapor pressure.

$$\frac{\partial \left(\varepsilon_g \tilde{\rho}_a \right)}{dt} = -\nabla \cdot \vec{J}_a \tag{6}$$

$$\frac{\partial \left(\varepsilon_g \tilde{\rho}_v \right)}{\partial t} + \frac{\partial \overline{\rho}_l}{\partial t} - \frac{\partial \overline{\rho}_d}{\partial t} = -\nabla \cdot \left(\vec{J}_v + \vec{J}_l \right) \tag{7}$$

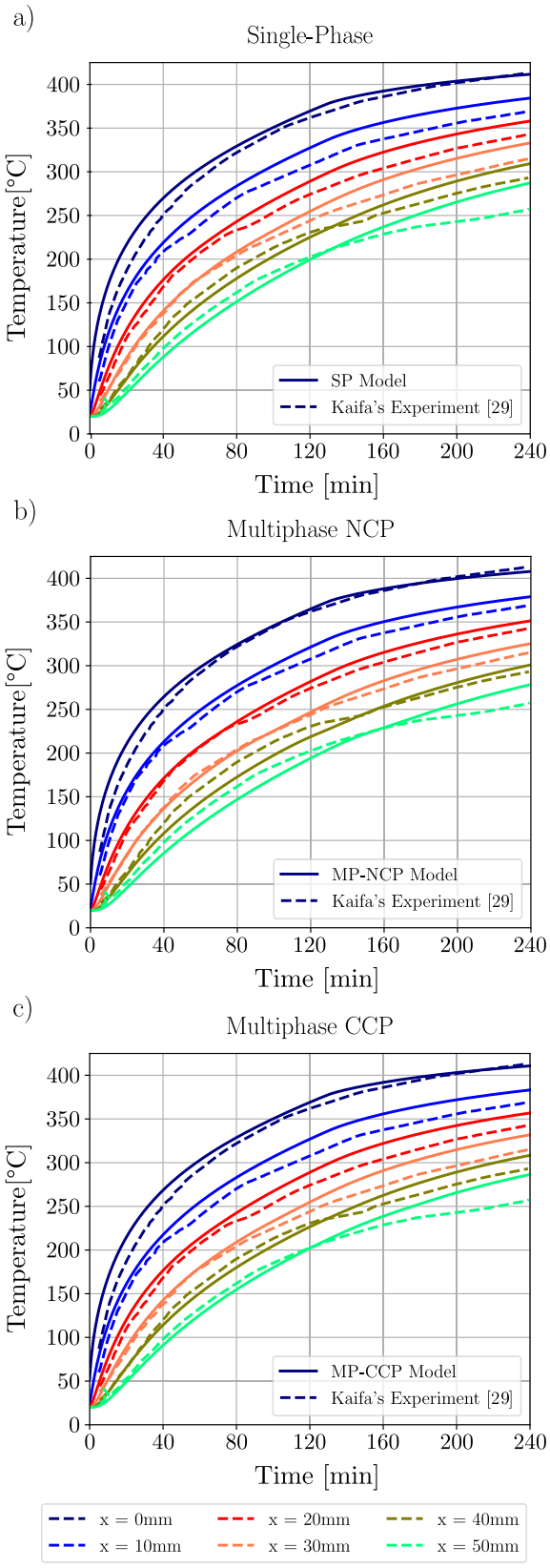

Fig. 7. Comparison of the temperature evolution predicted by the models with the PTM tests reported in Ref. [30]. In (a), SP represents the single-phase model (Section 2.2), in (b), MP-NCP stands for the multiphase model neglecting capillary effects (Section 2.3), and in (c), MP-CCP denotes the multiphase model considering the capillary pressure (Section 2.4).

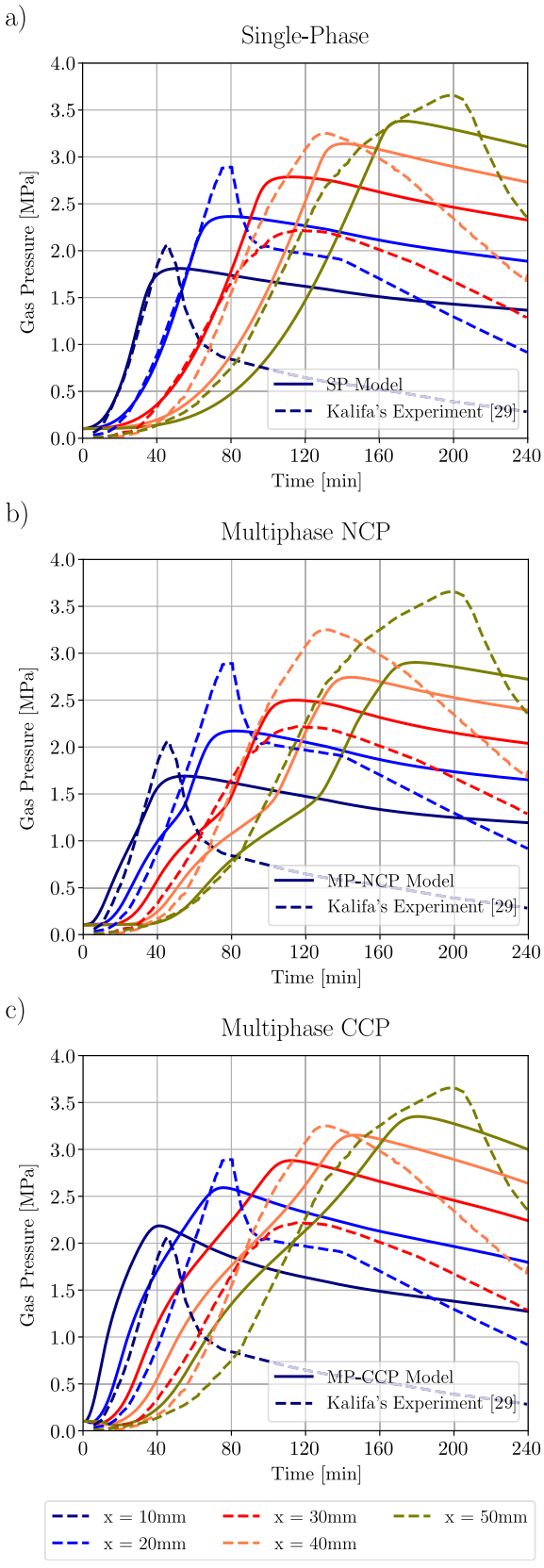

Fig. 8. Comparison of the gas pressure evolution predicted by the models with the PTM tests reported in Ref. [30]. In (a), SP represents the single-phase model described in Section 2.2, in (b), MP-NCP stands for the multiphase model neglecting capillary effects, as defined in Section 2.3, and in (c), MP-CCP denotes the multiphase model considering the capillary pressure, as shown in Section 2.4.

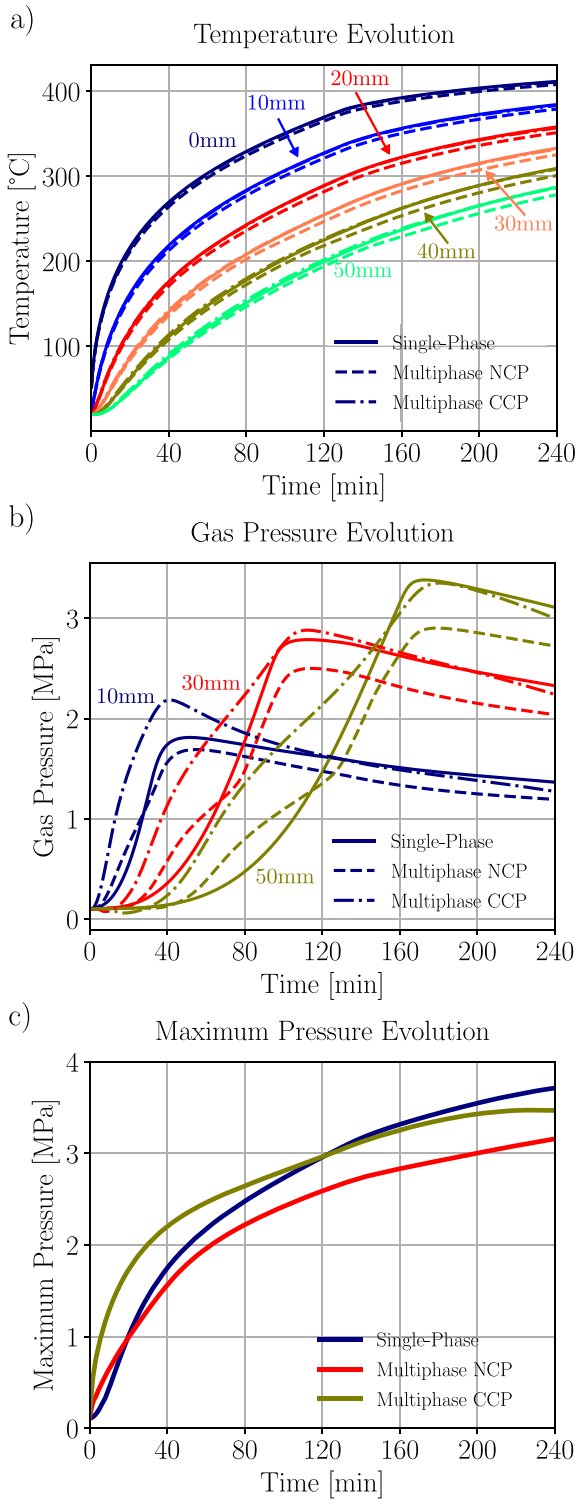

Fig. 9. Summary of the comparison among the models regarding the temperature evolution (a), the gas pressure evolution (b) and the maximum pressure evolution (c) of the PTM tests.

$$\left(\overline{\rho C_p}\right)\frac{\partial T}{\partial t} - \Delta H_{vap}\frac{\partial \overline{\rho}_l}{\partial t} + \left(\Delta H_d + \Delta H_{vap}\right)\frac{\partial \overline{\rho}_d}{\partial t} = \nabla\cdot(\lambda\nabla T) + \Delta H_{vap}\nabla\cdot\vec{J}_l - \left(\overline{\rho C_p\,\vec{v}}\right)\cdot\nabla T \tag{8}$$

Equations (6)–(8) describe the mass balance of dry air, of humidity (liquid water and vapor) and the thermal energy balance. The dry air mass flux, $\vec{J}_a$ is given by the Darcy and diffusion mechanisms as

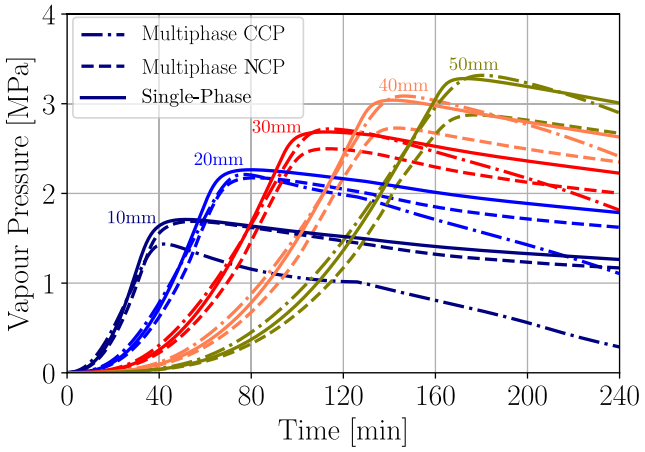

Fig. 10. Evolution of the vapor pressure predicted by the models during the PTM test.

described in Equation (9), where the symbols are defined in the nomenclature index. The mass flux of vapor is assumed in a similar way, only changing the densities of the phases considered, i.e.:

$$\vec{J}_a = -\varepsilon_g\tilde{\rho}_a\frac{KK_gK_k}{\mu_g}\nabla p_g - \varepsilon_g\tilde{\rho}_g D_{AV}\nabla\left(\frac{\tilde{\rho}_a}{\tilde{\rho}_g}\right) \tag{9}$$

$$\vec{J}_v = -\varepsilon_g\tilde{\rho}_v\frac{KK_gK_k}{\mu_g}\nabla p_g - \varepsilon_g\tilde{\rho}_g D_{AV}\nabla\left(\frac{\tilde{\rho}_v}{\tilde{\rho}_g}\right) \tag{10}$$

The mass flux of liquid is also given by both a Darcy term and one that represents the diffusion of the adsorbed water. The former resembles the first term of the right hand side of Equations (9) and (10), considering the properties and the pressure of the liquid phase instead of the gas one.

$$\vec{J}_l = -\overline{\rho}_l\frac{KK_l}{\mu_l}\nabla p_l - \overline{\rho}_l D_b\nabla S_b \tag{11}$$

The adsorbed water diffusion is considered by the last term of the right hand side of Equation (11), where ∇S_b represents the sorptive bound water and is given by Ref. [23]:

$$\nabla S_b = \left\{\begin{array}{ll}\nabla S, & \text{if } S \le S_{ssp}\\ 0, & \text{if } S > S_{ssp}\end{array}\right\} \tag{12}$$

The solid saturation point, S_{ssp}, defines the degree of saturation limit where there is only physically bound water (and no capillary water) below it.

The boundary conditions applied in this formulation are related to the primary variables selected, the temperature and the dry air and the vapor pressures. Considering the heat transport, both conditions described by Equations (3) and (4) (the convection and radiant heat transfer, respectively) can be applied, as well as the definition of specific temperatures at the boundary via the Dirichlet boundary condition (DBC) [23].

The dry air transport at the edges of the computational domain can also be modeled by DBC (such as the ones applied by Fey et al. [23]), or as a mass flux as follows

$$\hat{\mathbf{n}}\cdot\vec{J}_a = h_a\left(\tilde{\rho}_a - \tilde{\rho}_{a,\infty}\right) \tag{13}$$

where $\tilde{\rho}_{a,\infty}$ is the density of the dry air of the environment and h_a is the mass transfer coefficient of dry air.

A similar approach can be applied for the vapor transport at the boundaries.

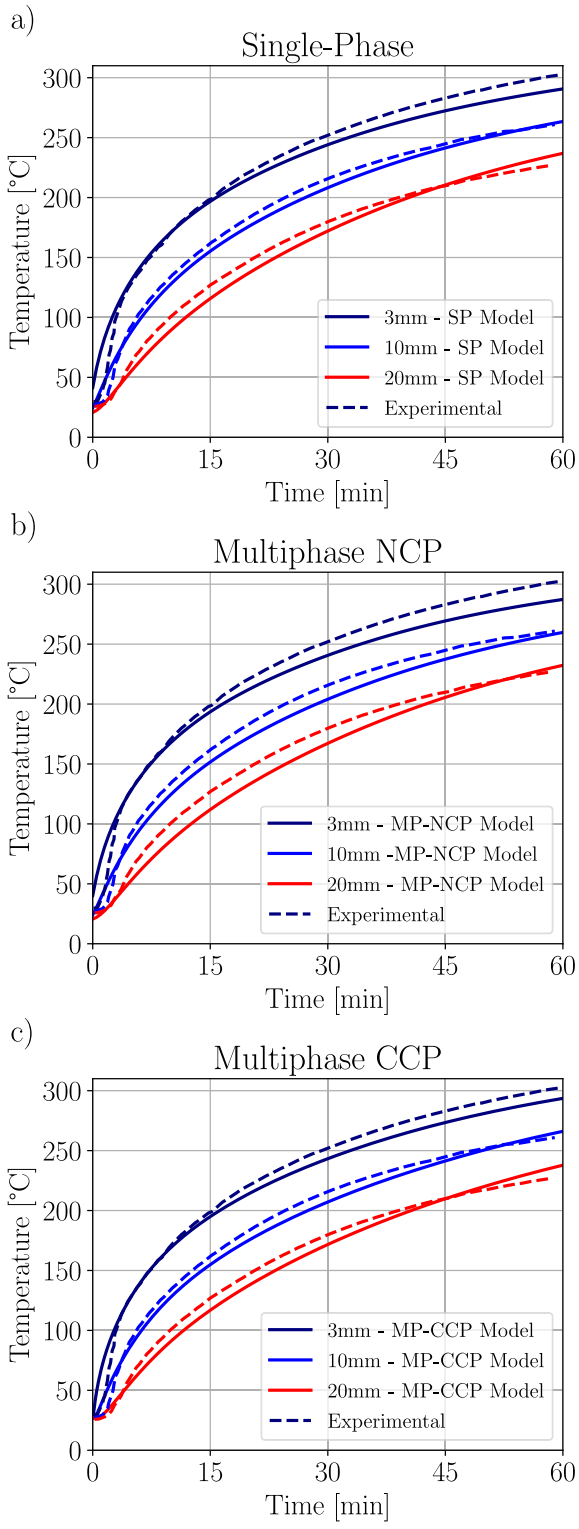

Fig. 11. Temperature evolution predicted by the models with the neutron tomography test reported in Ref. [43]. In (a), SP represents the single-phase model, in (b), MP-NCP stands for the multiphase model neglecting capillary effects, and in (c), MP-CCP denotes the multiphase model considering the capillary pressure.

$$\hat{\mathbf{n}} \cdot \vec{J}_v = h_v \left(\tilde{\rho}_v - \tilde{\rho}_{v,\infty} \right) \tag{14}$$

Again, the approach taken by Fey et al. assumed fixed values at the edges using a DBC. It should be noted that this choice of fixing both P_a and P_v guaranteed that the total gas pressure at the boundaries were equal to the atmospheric one. The value related to the vapor pressure was defined by the ambient relative humidity [23]. Moreover, it is important to emphasize that the liquid pressure, described in Equation (11), is taken as equal to the gas pressure. This is equivalent to consider that there is no effect of the capillary pressure due to the surface tension among the multiple phases involved [23].

There is no clear explanation in the literature justifying this modeling approximation, and it could be related to the selection of the primary variables. Gawin et al. reported that using the capillary pressure itself as a primary variable had the advantage of being a quantity that could have physical meaning attributed to it, both at low and high temperatures [8]. It was also reported that the simplification of neglecting the capillary effects yielded a model with inconsistent assumptions [15,40,41].

Thus, the next model to be presented follows the strategy proposed by Gawin et al. and considers the effect of capillary pressure. On the other hand, the effect of the adsorbed water mass transport is neglected, and the primary variables used are also different. The given nomenclature considering or neglecting the capillary effects is used to highlight what the fundamental difference is between such multiphasic models, but one should notice that this is not the only difference between them.

2.4. Multiphase model considering capillary effects

A more theoretically consistent approach for multiphase models is given by considering the capillary pressure effect on the liquid pressure and its use as one of the primary variables, as firstly proposed by Gawin et al. [20], and also adopted by Dal Pont et al. [32,42] (consequently referenced as MP-CCP). It was shown that such a strategy respects the thermodynamic laws (specifically obeying Kelvin's law for capillary pressure, as all phases are considered under thermodynamic equilibrium) by considering a different meaning of this capillary pressure for regions where there is no liquid water [21].

The mass balance is given by Equations (15) and (16), whereas the thermal energy one is described in Equation (17).

$$\frac{\partial(\varphi(1-S_l)\tilde{\rho}_a)}{\partial t} = -\nabla \cdot \vec{J}_a \tag{15}$$

$$\frac{\partial(\varphi S_l \rho_l)}{\partial t} + \frac{\partial(\varphi(1-S_l)\tilde{\rho}_v)}{\partial t} - \frac{\partial \rho_l}{\partial t} = -\nabla \cdot \left(\vec{J}_v + \vec{J}_l \right) \tag{16}$$

$$\left(\overline{\rho C_p}\right)\frac{\partial T}{\partial t} - \Delta H_{vap}\frac{\partial(\varphi S_l \rho_l)}{\partial t} + \left(\Delta H_d + \Delta H_{vap}\right)\frac{\partial \overline{\rho}_d}{\partial t}$$

$$= \nabla \cdot (\lambda \nabla T) + \Delta H_{vap} \nabla \cdot \vec{J}_l - \left(\overline{\rho C_p \vec{v}}\right) \cdot \nabla T \tag{17}$$

The first equation corresponds to the mass balance of dry air. The difference regarding Equation (9) is that the fraction of gas, ε_g, was replaced by the product between the porosity and the volume fraction of gas, φ and $(1 - S_l)$, respectively. The air flux is given by Equation (9), however the Klinkenberg correction is neglected.

The vapor flux in the mass balance equation of humidity is also described in a similar manner. The main difference is in the flux of water described in Equation (18), where the Klinkenberg factor and the diffusion of adsorbed water are neglected.

$$\vec{J}_l = -\overline{\rho}_l \frac{K_l}{\mu_l} \nabla p_l \tag{18}$$

The definition of the liquid pressure is also distinct. Instead of assuming that it is equivalent to the gas pressure, the capillary pressure is accounted for and the gradient of the liquid pressure is given by,

$$\nabla p_l = \nabla p_g - \nabla p_c \tag{19}$$

For the boundary conditions, once more the thermal conditions can

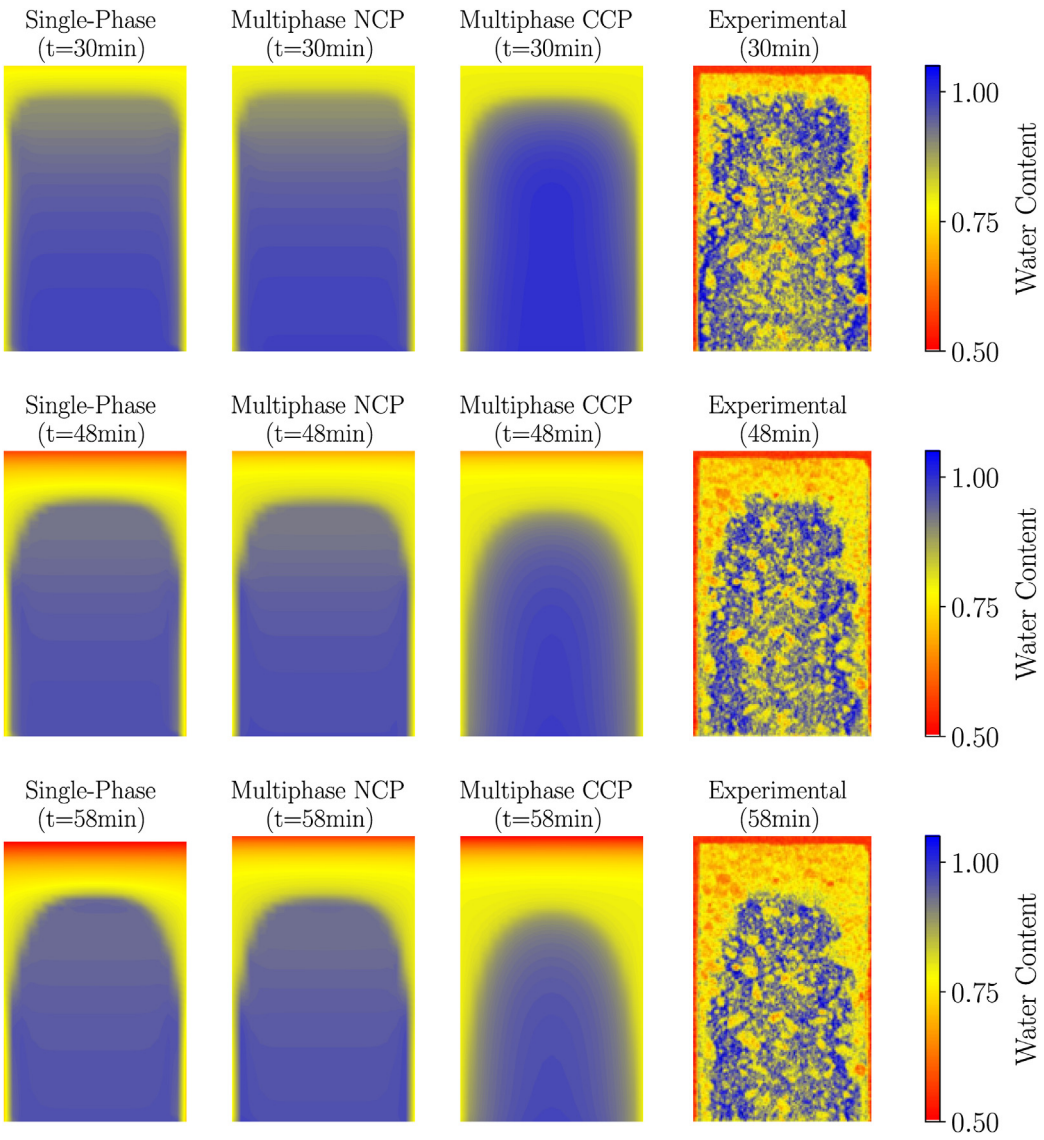

Fig. 12. Comparison of the relative water change predicted by the models with the neutron tomography test reported in Ref. [43].

be of the Dirichlet type or the Robin one, as given by Equations (3) and (4).

The gas pressure is often fixed as the atmospheric pressure through Dirichlet conditions [32,42], but an expression similar to the one described in Equation (14) can also be applied, which is also used as the boundary condition for the mass balance equation of water.

2.5. Benchmark cases

The benchmark cases are divided into two different types of experiments. Firstly, the results reported by Kalifa et al. [30], where pressure and temperature measurements were obtained during one dimensional heating of a slab of Portland cement concrete (also known as the TM test). The selected properties of the concrete are taken from Dauti et al. [43]. The setup is shown in Fig. 2.

Secondly, a neutron tomography test was also considered. The properties of the high performance concrete composition analyzed through the neutron tomography were obtained from a previous set of studies [32]. These properties of the selected material can be found in Appendix A. The setup is depicted in Fig. 3.

3. Results and discussion

The current section is divided into two parts. The first one is devoted to the validation of the current finite element implementation of the three different models (single-phase, MP-NCP and MP-CCP), previously introduced (Sections 2.2, 2.3, 2.4). This is accomplished by comparing the attained results with those previously published for each model. Although this step is of utmost importance, its completion is complicated by the fact that some of the input parameters are not clearly reported in the literature and because the numerical strategies are different and are also not often reported in detail.

The second part of this section presents the comparison with experimental results based on both temperature and pressure measurements during heating, collected by sensors placed within the samples (as shown by Kalifa et al. [30]) and the measurements of moisture content obtained by neutron tomography tests (described by Dauti et al. [31,43]).

3.1. Validation of the finite element implementations

3.1.1. Single-phase model

The single-phase model developed by Bažant et al. was validated with the results obtained by Gong et al. [17]. The simulated case represents a

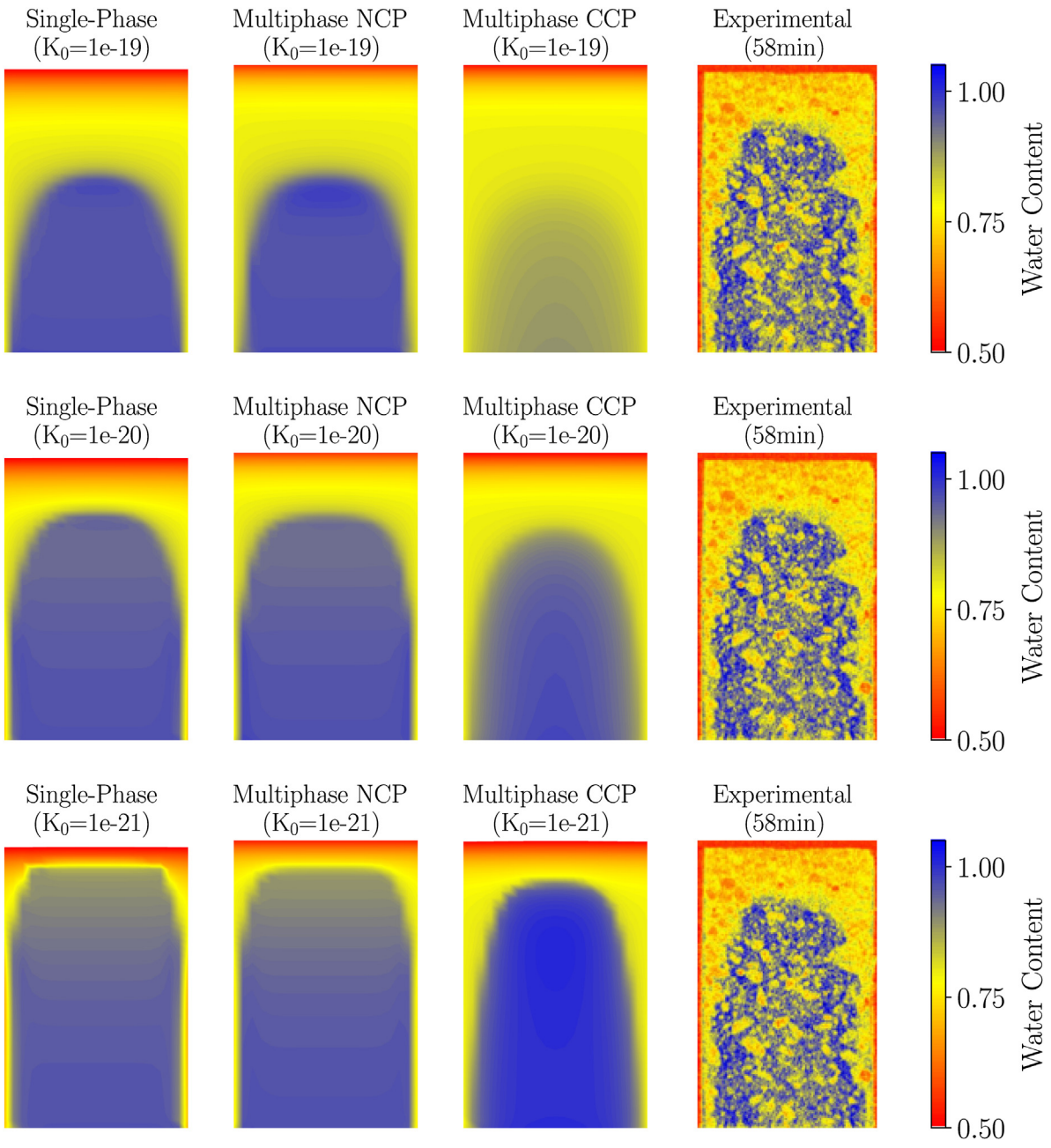

Fig. 13. Comparison of the models' sensitivity to the initial permeability, K_0 (m^2), after 58 min of heating. The neutron tomography test reported in Ref. [43] is also presented for comparison.

refractory castable wall of 20 cm submitted to a heat-up curve that comprises two constant heating rate regimes (30°C/min) and a temperature plateau (200°C for 10 h). The unidimensional mesh was defined with 40 elements and the time step was 15 s, as reported by Gong et al. For more information the reader is referred to the original work [17].

Besides the properties of the material, several details about the numerical aspects are also described in Ref. [17], such as the use of a predictor-corrector method for solving the nonlinear equations and the strategy for numerically differentiating the sorption isotherms with the help of a central formulation based on the results of successive time steps.

In this work, the solution of the discretized problem was obtained via linearizing its resulting equations. The numerical derivatives of the sorption isotherm were obtained using a central difference scheme that was independent of the time step, as described in Equation (20) (a similar expression is used for differentiating the sorption isotherm with respect to the temperature and in the current implementation $\delta_p = \delta_T$).

$$\frac{\partial \overline{\rho}_l(T^n, p^n)}{\partial p} \approx \frac{\overline{\rho}_l(T^n, p^n + \delta_p\, p^n) - \overline{\rho}_l(T^n, p^n - \delta_p\, p^n)}{2\,\delta_p\, p^n} \tag{20}$$

where $\delta_p \ll 1.0$ is a parameter that defines how refined the approximation of the sorption isotherm is. In the numerical studies developed by the present authors, it was found out that reducing this parameter could increase the predicted maximum pressure by almost 20%, when compared with the strategy adopted by Gong et al. [17]. A rough estimation of an equivalent value of δ_p for Gong's approach (considering the results of successive time steps) yields a numerical differentiation with the parameter close to $\delta_p = 1.0 \times 10^{-3}$. For δ_p values smaller than 1.0×10^{-6}, the results converged to those with higher pressures.

Fig. 4 shows a comparison among results considering Gong et al. and the finite element implementation developed herein.

The temperature profiles shown in Fig. 4 (a) are close to those

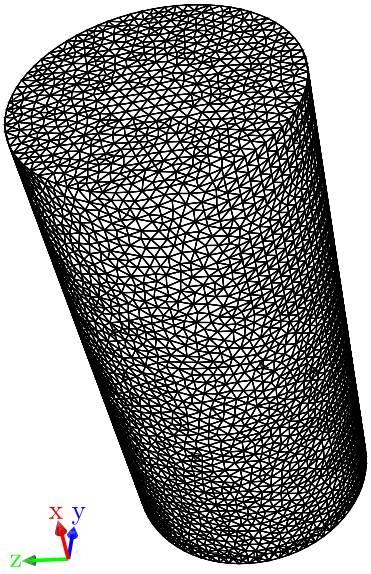

Fig. 14. Mesh used in the 3D simulations.

reported in the original work [17], specially close to the heated face.

Some larger differences are observed on the cold side, which could be related to using a different numerical strategy and also to the boundary condition adopted. The boundary condition described in Ref. [17], presented in Equation (21), comprises a term related to the thermal energy transport due to the flux of mass. In the present implementation, when this term was considered, it resulted in temperature profiles with no physical meaning and that were considerably different from the ones presented in the original work. Therefore, it was neglected.

$$-\hat{\mathbf{n}} \cdot \lambda_{eff} \nabla T = h_T (T - T_\infty) + C_{p,l}\, h_m (P - P_\infty) \tag{21}$$

The pressure profiles described in Fig. 4 (b), which are highly affected by the strategy adopted to differentiate the sorption isotherm, shows a good correspondence with the values described in the work by Gong et al., when $\delta_p = 0.005$ was used (i.e. using values of the same order of magnitude of the estimated parameter δ_p that was equivalent to Gong's strategy).

This agreement can also be seen in the maximum pressure evolution in Fig. 4 (c). The highest difference was around 6 and 18 h, and is possibly related to the strategies adopted here to solve the problem (linearizing the equations by explicitly using the primary variables of the last time step for the material property functions instead of using the predictor-corrector originally proposed) and the numerical derivative of the sorption isotherm (by using Equation (20)).

Table 1
Comparison of the computational cost of the three models regarding the CPU time for running the 3D neutron tomography simulations. All computations were performed using a desktop Intel Xeon E3-1225 (3.30 GHz) with 16 Gb RAM. The results presented are on a comparative basis as such timings can vary depending on other factors such as other sub-processes carried out during the simulation.

	Single-Phase	Multiphase NCP	Multiphase CCP
CPU Time	75% Faster (≈ 10min)	Slowest (≈ 45min)	10% Faster (≈ 40min)

The possible sources of differences between the finite element implementation of the current work and the results from Gong et al. [17] are summarized next:

- Use of a central difference scheme independent of the time discretization for differentiating the sorption isotherm with respect to the temperature and pressure;
- Use of a linearized system of equations instead of the predictor-corrector method described in Ref. [17];
- Neglecting the thermal boundary condition related to the thermal energy transport due to the mass flux (second term of the right hand side of Equation (21)).

Altogether, it can be concluded that the finite element implementation via FEniCS platform of Bažant's model proposed in the present work yields similar results and qualitatively agrees with those reported in the work by Gong et al., therefore it is validated for further investigations.

3.1.2. *Multiphase model neglecting capillary effects*

The finite element implementation into the FEniCS platform of the thermohygro model neglecting capillary effects was validated by comparing it with the results reported by Fey et al. [23]. The simulation consists of a 1D wall of refractory castable heated from the left side. More details can be found in the original publication [23], where the model is discretized using the finite difference method and the upwind scheme. The possible differences due to the use of the Finite Element Method could be one source of variation among the results. Likely errors in reporting the properties could also be a reason for the discrepancies, as the work described in Ref. [23] presents two different set of results with distinct materials.

One critical point is related to the sorption isotherm adopted by Fey et al., whose analytical expression disagrees with its plot (comparing

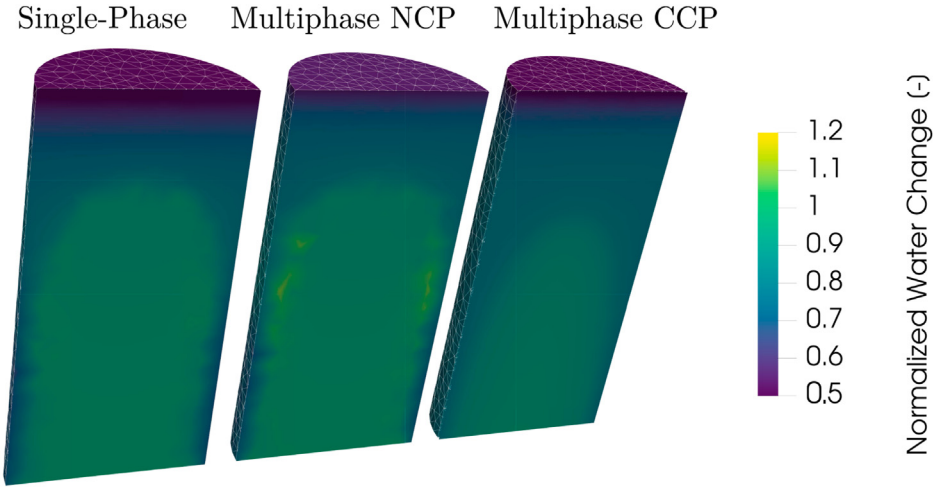

Fig. 15. Water content at the end of the simulation for the 3D analysis.

Figure B31 and Equation B17 shown in Ref. [23], one concludes that the upper limit of the sorption isotherm is 0.95 instead of 0.9). In private communications with the corresponding author of [23], some of the issues were solved, such as the use of 0.95 as the correct factor for the sorption isotherm and also the intrinsic permeability used, yielding the results described in Fig. 5.

Again, there is a very good agreement in the temperature evolution as seen in Fig. 5 (a), pointing out that the thermal properties reported and the energy balance equations implemented are all equivalent.

The gas pressure evolution shows a reasonable fitting, both on the pressure peak time and the overall value (Fig. 5 (b)). The main difference (roughly 0.2 MPa) was detected for the pressure evolution at 12 cm from the heated face.

Finally, in Fig. 5 (c), the behavior of the dry air gas pressure is compared, showing a great match until the 21h mark, where the finite implementation developed in this work predicts a steeper increase in the pressure values.

These results show good overall agreement between both implementations validating our computational tool.

3.1.3. Multiphase model considering capillary effects

Finally, the multiphase model comprising the capillary effect was analyzed and compared with the results by Dauti and Weber [43,44], where the simulation of a 1D domain of concrete heated by thermal radiation and convection on the left side was assumed. This setup was used in the original works for validation of the thermohygro models as it represents the experimental test conducted by Kalifa et al. [30], which is also adopted as a benchmark in the next section.

The comparison among the results of the original works and the current finite element implementation is shown in Fig. 6.

Both temperature and pressure profiles show good agreement, with minor deviations, which could be derived from using different numerical solver procedures, or round-off differences of the coefficients of the input parameters.

This indicates that the implementation of the multiphase model considering the capillary effects is also properly carried out in the current work. Thus, equipped with all the three models, the next section compares experimental benchmarks with each one of the numerical implementations.

3.2. Experimental benchmarks

3.2.1. Temperature and pressure sensor results

PTM tests are broadly used as a benchmark for numerical models of concrete at high-temperatures [23,35,45,46]. These results are also applied to tune the physical parameters.

The current section aims to compare the behavior of distinct models, and, as they result from different initial assumptions, it is expected that each model would require its own set of tuning. Thus, the proposed methodology consists of using the same set of properties described in Appendix A (and based on [43]) for all three models and comparing these results to the experimental values. Considering this, the reader should keep in mind that the accuracy of such models could be improved by following the same approach that various authors have taken by adjusting the properties for each model (which was not carried out in this work).

Fig. 7 shows the comparison of the temperature evolution experimentally measured and the values predicted for the simulations, by the single-phase model, the multiphase one that neglects the capillary effects (NCP) and also the full multiphase thermohygro model (CCP), in (a), (b) and (c), respectively.

It can be observed that the measured temperature increase in the heated face matches the predicted values for all three models. At the following inner positions (10 mm, 20 mm, 30 mm, and 40 mm), the overall shape of the profile is well represented and the highest difference at the end of the experiment (240 min) is of roughly 15 °C (4%). The innermost position (50 mm) is the one with the most significant discrepancy, 35 °C (9.3%). The model that best described the evolution was the multiphase one that neglects the capillary pressure, where the most noticeable difference was around 20 °C (5.3%).

Considering the pressure development, Fig. 8 shows the comparison of the models with the values experimentally measured. The single-phase model does not provide the gas pressure result directly, and thus, the value used is the sum of the predicted vapor pressure and the atmospheric one (0.101325 MPa). It can be concluded from Fig. 8 (a) that the predicted pressure profiles match the experimental values for the positions closer to the hot face (10 mm, 20 mm and 30 mm).

However, the pressure peak calculated for all analyzed conditions is smaller and the following decrease is not as intense as the measured values. This is explained by the fact that the mechanical effect of the permeability increase was not considered [35,43,44]. Finally, the moment where the pressure peak reaches its maximum value is also satisfactorily predicted, only showing a difference for the 50 mm position. Another change observed is related to the results at 30 mm, where the experimental values are lower than the ones predicted by the models. This can be explained by problems with the sensor used at this position, as reported by Kalifa et al. [30].

Regarding the multiphase model that neglects the capillary pressure, presented in Fig. 8 (b), the pressure peaks predicted are lower. During the first minutes, higher values than the ones obtained experimentally are observed from the numerical simulation. Again, the exception is the 30 mm position, where the experimental values are doubtful.

Finally, the multiphase thermohygro model comprising the capillary pressure is the one that best represents the experimental values, considering both the pressure peak position and its value (for example at the 10 mm position, predicting a peak of 2.1 MPa after 40 min of heating). This is also a consequence of the fact that the input properties for all the models evaluated were the ones reported by Dauti et al. [43], who also used the multiphase model that considers the capillary effects. Thus, such parameters were adjusted for this model, which justifies its better behavior.

Fig. 9 (a) shows the temperature evolution for the three models in a single graph. It can be observed that they are equivalent. Only the multiphase model that does not consider the capillary pressure shows lower temperatures.

When comparing the gas pressure evolution of all models (Fig. 9 (b)) it is evident that the differences among the results are less than 20% considering the attained maximum peak values, indicating that although the starting hypothesis are considerably distinct, the overall results are similar. This can also be seen in the evolution of the maximum gas pressure values (Fig. 9 (c)).

One of the likely explanations for such differences of the gas pressure is related to the share of the dry air pressure (as $p_g = p_a + p_v$). To check this hypothesis, Fig. 10 presents the evolution of the vapor pressure (a quantity that is calculated for all models).

The highest difference was detected at the positions closer to the heated face (10 mm and 20 mm) at later times (after 40 min), which are the ones that were already dried and where the effect of the capillary pressure is most pronounced. At the other positions and moments, the difference is negligible comparing all three models.

From a technological application point of view, such specificities could be considered not significant for justifying the use of models of higher complexity, specially when considering that each model can be properly finely tuned according to the experimental results (whereas for this set of results they all share the same input parameters).

Considering the limitations of the PTM tests (see Section 2.1), the next section aims to conduct the comparison of the models using the results of the moisture fields obtained by the neutron tomography tests.

3.2.2. Neutron tomography results

Firstly, the temperature evolution at three specific positions inside the cylindrical sample were measured using thermocouples. The comparison

with the values predicted by the models is shown in Fig. 11.

It can be observed that all three approaches show a similar trend, where there is a good agreement for the first 15 min at the 3 mm position, but afterwards, the model predicts lower values. The biggest difference was detected upon completion of the test, where it is roughly 12°C. The values at position 10 mm and 20 mm shows an opposite trend, where the matching between the experimental and numerical results is better at later stages. Considering these and also the earlier results from the PTM benchmark (Section 3.2.1), it can be concluded that all three approaches showed equivalent thermal results.

In the work by Dauti et al. [32,43], it was pointed out that the beam hardening effect due to radial moisture flux affected the calculations of the water content. Efforts to minimize this effect are still under development [47], but to this point, this remains an issue for this technique. Thus, the next set of comparisons will be based on qualitative analysis of the moisture content field throughout the samples. Further quantitative studies considering the performance of the different modelling approaches will be carried out when the beam hardening effect will be correctly prevented, resulting in new experimental quantitative results. In the meantime, the qualitative analysis is presented next.

Fig. 12 shows the comparison of the relative water change between two moments predicted by the models and the one obtained by the neutron tomography tests. This quantity is calculated by Equations (22) and (23), where φ is the porosity of concrete, S_l is the saturation with liquid water, ρ_l is the density of liquid water, m_{dehyd} is the mass of water released due to dehydration and w_i is the initial water content (for this concrete composition, $w_i = 189.1 \text{kg/m}^3$)

$$w_{\text{change}} = (\varphi S_l \rho_l)_0 - (\varphi S_l \rho_l)_t + \Delta m_{\text{dehyd}} \tag{22}$$

$$\widehat{w}_{\text{change}} = \frac{w_i - w_{\text{change}}}{w_i} \tag{23}$$

It can be observed that the drying front has the same velocity (compare the height of the blue blunt front) for all the three models, which agree with the experimental results observed. The single-phase and multiphase NCP results are equivalent, whereby the biggest difference is that the drying at the hot face is more intense in the former. The multiphase CCP has a steeper drying front, highlighting that the lateral drying predicted is higher than the other models, which can be explained by the capillary pressure effects.

Overall, all three models resulted in qualitatively equivalent predictions, which agree with the overall behavior of concrete observed by neutron tomography.

Considering this qualitative equivalence between the water content prediction, one important aspect that remains to be analyzed is the sensitivity of the models to the initial intrinsic permeability, K_0. In order to investigate this aspect, simulations with the three approaches were carried out assuming $K_0 = 10^{-19}$ m^2, $K_0 = 10^{-20}$ m^2 (the default values) and $K_0 = 10^{-21}$ m^2.

Based on the obtained results (Fig. 13), reducing the initial permeability decreases the drying front speed (bottom row results), conversely, when this parameter is increased, the water removal takes place faster (top row results). This trend can be observed for all models. Moreover, the initial intrinsic permeability of 10^{-20} m^2 is the one that best represents the actual water removal, as lower values predict faster drying than the one observed by the neutron tomography, and higher ones results in slower water withdrawal.

Comparing each modelling approach, one can see that again both single-phase and multiphase NCP models are analogous, showing a small difference of the water accumulation (the phenomenon also known as moisture clog) at the inner colder positions of the sample. These profiles are different than those predicted by the multiphase CCP model, where the water accumulation is very sensitive to the initial intrinsic permeability, predicting a noticeable content of water ahead of the drying front in the case of the material presenting the lowest permeability (case with $K_0 = 10^{-21}$ m^2, at the positions in dark blue). Again, this specific behavior of the MP-CCP model could be associated to the capillary pressure effects.

Finally, one last comparison among the models was carried out using a 3D mesh of the neutron tomography experiment setup. The objective was to compare the computational cost of such models in situations where this is a limiting factor. The mesh used has 12879 tetrahedral elements and 2811 nodes and is shown in Fig. 14.

Fig. 15 presents the results of the water content in the 3D case after completing the simulation. There are no major differences when comparing such values with the prediction of the bi-dimensional models (Fig. 12). Despite the differences among the distinct modelling approaches, similar results for the single-phase and multiphase CCP models were observed, with the main difference being the higher lateral drying and the water accumulation ahead of the drying front predicted by the latter.

Table 1 shows the CPU time for the simulations. It was observed that the single-phase model was over three times faster than the other approaches. This was expected because of the fewer number of degrees of freedom (DOF) of this model when compared to the multiphasic options (in fact, it comprises two thirds of the DOF of the multiphase models for the same mesh, type and order of the finite elements), as it considers only two primary variables instead of the three needed for defining the other cases. Neglecting the capillary pressure resulted in the longest simulation time indicating that numerical efficiency is not a strong argument to disregard the capillary pressures at the cost of the theoretical consistency.

Thus, specially considering optimization algorithms where a large number of numerical experiments need to be run, the single-phase model can be of great interest, reassuring its technological application attribute. For the case of defining a heating procedure for a refractory castable lining, for example, an initial screening might be carried out with the single-phase tool and the best candidates can be simulated using the CCP multiphase approach, assuming that all the needed parameters are known.

In summary, in the present work all three selected models were implemented and validated with the results reported in the original works that described such procedures. Minor deviations were detected, and thus it was possible to assume that the implementations of these models using the FEniCS open source framework were correctly carried out.

The first set of comparisons used the well-established PTM tests conducted by Kalifa et al., where the pressure and temperature evaluations were obtained at specific positions. All three models were able to reproduce the temperature evolution with a margin of error lower than 35°C (9.3%). The model that neglected the capillary pressures (NCP) performed slightly better than the others (where the highest error was 20°C, 5.3%). When considering the gas pressure predictions, the NCP model was the one with the highest difference, predicting lower values for the pressure peaks (roughly 20%). The single-phase approach (SP) was closer to the multiphasic one that included the capillary effects (CCP), which best represented the experimental results. Finally, the vapor pressure prediction of all models showed a very similar behavior, specially at the innermost positions of the concrete specimens. The exception was the multiphase CCP model at the position close to the samples' boundary, pointing out that the capillary effects are more pronounced in such regions.

The comparison with the neutron tomography data was carried out both considering the temperature evolution and the qualitative behavior of the water content inside the sample. Again, the temperature increase profile was equivalent for all the models. The water content results supported the finding that the capillary effects are most noticeable at the boundary, as this was one of the biggest difference from the other approaches. Another distinction was the more intense water accumulation ahead of the drying front predicted by the multiphase CCP model.

When assessing the sensitivity of the models to the initial intrinsic

permeability, it was identified that its effect on the speed of the drying front is the same for all models, and the only difference was that when using lower values of this parameter only the multiphasic approach that considered the capillary effects (CCP) resulted in increased water accumulation.

Finally, the evaluation of the neutron tomography test using a 3D mesh was also conducted to compare the computational cost of the different approaches. It was observed that the SP model (which yields the lowest number of degrees of freedom as it considered only two primary variables) was roughly three times faster than the multiphasic ones. The computational costs of the multiphase models with or without the capillary pressure were similar.

4. Conclusions

The present study aimed to extend the understanding of the numerical models used to simulate refractory castables and concrete upon heating by directly comparing the results of the most well-known options available in the literature with experimental tests. This contribution is unprecedented as most of the earlier comparisons available were based only on theoretical discussions without considering a benchmark case and actually implementing the distinct approaches using the same finite element platform.

Based on these findings a clear picture can be drawn of such approaches providing important information for end-users that might adopt one of these strategies. The most complete multiphasic model (CCP) has a stronger theoretical consistency, and is capable of providing more details of the behavior of the porous media at higher temperatures. The NCP showed no computational cost advantages nor was it capable of detecting features such as the increased water accumulation ahead of the drying front. The simplest single-phase approach (SP) yields comparable results to the multiphasic models, and is simpler and more computationally efficient at the cost of some theoretical concepts and capability to represent the complete behavior of the material.

Consequently, from a technological application point-of-view, the SP model would be the best one suited for practical scenarios of modeling the drying of numerous distinct refractory castables, as the properties of such materials vary considerably even with small changes on their compositions, which ultimately hinders the application of more complex multiphasic approaches that demand multiple input parameters.

Declaration of competing interest

The authors declare that they have no known competing financial interests or personal relationships that could have appeared to influence the work reported in this paper.

Acknowledgments

This study was financed in part by the Coordenação de Aperfeiçoamento de Pessoal de Nível Superior - Brasil (CAPES) - Finance Code 001. The authors would like to thank Conselho Nacional de Desenvolvimento Cientifico e Tecnologica – CNPq (grant number: 303324/2019-8 and 132342/2020-0) and Fundação de Amparo à Pesquisa do Estado de São Paulo - FAPESP (grant number: 2019/07996-0) for supporting this work. The authors are also grateful to the support from FIRE and Imerys.

Appendix A. Properties of the HPC material

Both the PTM and neutron tomography experimental tests used for the benchmarks in this paper were applied to Portland cement concrete. The properties used for the simulations of such tests are the same as the ones reported in the original works [32,43,44] and are also presented next.

Appendix A.1. Material considered in PTM tests

The PTM test reported by Kalifa et al. were conducted using a high performance concrete, MT100. The initial properties are listed in Table A.1.

Table A.1
Summary of properties of the MT100 high performance concrete used for modelling the PTM tests reported by Kalifa et al. [30].

Property	Value
Initial Solid Density, $\rho_{s,0}$	2611 kg/m^3
Solid Density Evolution, $\rho_s(T)$	Equation A.1
Initial Porosity, φ_0	0.1368
Porosity Evolution, $\varphi(T)$	Equation A.2
Initial Specific Heat of Solid, $C_{p,s,0}$	948 J/kgK
Specific Heat of Solid, $C_{p,s}(T)$	Equation A.3
Initial Dry Thermal Conductivity, $\lambda_{d,0}$	1.67 W/mK
Thermal Conductivity Evolution, $\lambda(T,S_l)$	Equation A.4
Initial Intrinsic Permeability, K_0	7.5x10^{-20} m^2
Intrinsic Permeability Law, $K(T,p_g)$	Equation A.6
Gas Relative Permeability, $K_g(T,S_l)$	Equation A.7
Liquid Relative Permeability, $K_l(T,S_l)$	Equation A.8
Dehydration Mass, $\frac{\partial \overline{\rho}_d}{\partial T}$	Equation A.9
Initial Relative Humidity, RH_0	0.5
Emissivity, ε	0.85
Retention Curves, $S_l(T,p_c)$	Equation A.11

$$\rho_s = \rho_{s,0} + A_{\rho,s}(T - T_0) \tag{A.1}$$

with $A_{\rho,s} = 0.2235$ and $T_0 = 273.15$ K.

$$\varphi(T) = \varphi_0 + A_{\varphi}(T - T_0) \tag{A.2}$$

where $A_\varphi = 0.78\text{x}10^{-5}$ K^{-1} and $T_0 = 273.15$ K.

$$C_{ps}(T) = C_{ps0}[1 + A_c(T - T_0)] \tag{A.3}$$

where $A_c = 0.35$ K^{-1} and $T_0 = 273.15$ K.

$$\lambda(T, S_l) = \lambda_d\left(1 + 4\frac{S_l\varphi\rho_l}{(1-\varphi)\rho_s}\right) \tag{A.4}$$

where λ_d is given by Equation A.5

$$\lambda_d = \lambda_{d0}[1 + A_\lambda(T - T_0)] \tag{A.5}$$

and $A_\lambda = -0.0005$ K^{-1}.

$$K\left(T, p_g\right) = K_0 \cdot 10^{A_T(T-T_0)}\left(\frac{p_g}{p_{atm}}\right)^{A_p} \tag{A.6}$$

where $A_T = 0.005$, $A_p = 0.368$ and $p_{atm} = 101325$Pa.

$$k_{rg} = \sqrt{1 - S_l}\left(1 - S_l^{1/A_S}\right)^{2A_S} \tag{A.7}$$

$$k_{rl} = \sqrt{S_l}\left(1 - \left(1 - S_l^{1/A_S}\right)^{A_S}\right)^2 \tag{A.8}$$

where $A_S = 0.6$ for both Equations A.7 and A.8.

$$\frac{\partial\overline{\rho}_d}{\partial T} = f_s f_m f_c f(T) \tag{A.9}$$

where $f_s = 200$kg/m^3, $f_m = 0.24$, $f_c = 0.4$ and $f(T)$ is given by Equation A.10.

$$f(T) = \begin{cases} 0, & \text{if } T < 105^\circ C \\ \dfrac{[1 + \sin(\pi/2(1 - 2\exp(-0.004(T - 105))))]2}{,} & \text{if } T > 105^\circ C \end{cases} \tag{A.10}$$

$$S_l = \left(\left(\frac{E(T)}{a(T)}p_c\right)^{\frac{b}{b-1}} + 1\right)^{-1/b} \tag{A.11}$$

where $E(T)$ represents the influence of temperature on the surface tension and is given in Equation A.12, whereas $a(T)$ represents the microstructural changes on the material during its heating, depicted by Equation A.13, and $b = 2.27$ is an empirical parameter.

$$E(T) = \begin{cases} \left[\dfrac{T_{crit} - T_0}{T_{crit} - T}\right]^N & \text{if } T < 374.15^\circ C \\ \dfrac{N}{z}E_0 T + \left[E_0 - \dfrac{N}{z}E_0(T_{crit} - z)\right] & \text{if } T \geq 374.15^\circ C \end{cases} \tag{A.12}$$

with $N = 1.2$, $z = 5$ and $E_0 = 1$ non-dimensional constants obtained empirically.

$$a(T) = \begin{cases} Q_3 & \text{if } T < 100^\circ C \\ (Q_3 - Q_2)\left(1 + 2\left(\dfrac{T - 100}{T_{cr} - 100}\right)^3 - 3\left(\dfrac{T - 100}{T_{cr} - 100}\right)^2\right) & \text{if } T \geq 100^\circ C \end{cases} \tag{A.13}$$

where $Q_3 = 18.62$MPa and $Q_2 = 7$MPa obtained experimentally.

It should be noted that both the single-phase model (SP) and the multiphase that neglects the capillary pressure (NCP) demand updates on the retention curves, as the capillary pressure is not a primary variable of such models. To evaluate the retention curves, an equivalent capillary pressure, $\widehat{p_c}$ is calculated by means of Equation A.14.

$$\widehat{p_c} = -\log\left(\frac{p_v}{p_{sat}(T)}\right)\frac{\rho_l(T)\,R\,T}{M_v} \tag{A.14}$$

Appendix A.2. Material considered for neutron tomography tests

Most of the properties of concrete analyzed using the neutron tomography tests share the same laws used for the MT100 high performance concrete, with some of the empirical parameters adjusted as described in Table A2 (the changed parameters are presented explicitly in the Table A.2, otherwise the value used is the same as the ones defined in the previous section Appendix A.1).

Table A.2
Summary of properties of the high performance concrete used for modelling the neutron tomography tests reported by Dauti et al. [32,43].

Property	Value
Initial Solid Density, $\rho_{s,0}$	2389.64 kg/m^3
Solid Density Evolution, $\rho_s(T)$	Equation A.1
Initial Porosity, φ_0	0.05
Porosity Evolution, $\varphi(T)$	Equation A.2 with $A_\varphi = 14 \times 10^{-5}$
Initial Specific Heat of Solid, $C_{p,s,0}$	940 J/kgK
Specific Heat of Solid, $C_{p,s}(T)$	Equation A.3
Initial Dry Thermal Conductivity, $\lambda_{d,0}$	1.67 W/mK
Thermal Conductivity Evolution, $\lambda(T,S_l)$	Equation A.4
Initial Intrinsic Permeability, K_0	1x10^{-20} m^2
Intrinsic Permeability Law, $K(T,p_g)$	Equation A.6
Gas Relative Permeability, $K_g(T,S_l)$	Equation A.7
Liquid Relative Permeability, $K_l(T,S_l)$	Equation A.8
Dehydration Mass, $\frac{\partial \overline{\rho}_d}{\partial T}$	Equation A.15
Initial Relative Humidity, RH_0	0.58035
Emissivity, ε	0.8
Retention Curves, $S_l(T,p_c)$	Equation A.11 with $Q_3 = 96.28$MPa, $N = 2.2$ and $b = 1.954$

$$\frac{\partial \overline{\rho}_d}{\partial T} = f_{NT} f(T) \tag{A.15}$$

where $f_{NT} = 149.3$kg/m^3 and $f(T)$ is given by Equation A.16.

$$f(T) = \frac{A}{1 + \exp(-((T-B)/C)} \tag{A.16}$$

with $A = 0.814$, $B = 304.30$ and $C = 10.475$.

References

[1] C. Schacht, Refractories Handbook, Mechanical Engineering, CRC Press, 2004, ISBN 9780203026328. https://books.google.com.br/books?id=8oI2plVDQxUC.

[2] A.P. da Luz, M.A.L. Braulio, V.C. Pandolfelli, Refractory Castable Engineering, vol. 756, Goller Verlag GmbH, Baden-Baden, 2015.

[3] M. Ozawa, S. Uchida, T. Kamada, H. Morimoto, Study of mechanisms of explosive spalling in high-strength concrete at high temperatures using acoustic emission, Construct. Build. Mater. 37 (2012) 621–628, https://doi.org/10.1016/j.conbuildmat.2012.06.070. ISSN 0950-0618.

[4] R. Jansson, Fire Spalling of Concrete: Theoretical and Experimental Studies, Ph.D. thesis, KTH Royal Institute of Technology, 2013.

[5] D. Wang, C. Shi, Z. Wu, J. Xiao, Z. Huang, Z. Fang, A review on ultra high performance concrete: Part II. Hydration, microstructure and properties, Construct. Build. Mater. 96 (2015) 368–377, https://doi.org/10.1016/j.conbuildmat.2015.08.095. ISSN 0950-0618, http://www.sciencedirect.com/science/article/pii/S0950061815303147.

[6] Z.P. Bazant, W. Thonguthai, Pore pressure and drying of concrete at high temperature, ASCE J. Eng. Mech. Div. 104 (5) (1978) 1059–1079.

[7] A.K. Abdel-Rahman, G.N. Ahmed, Computational heat and mass transport in concrete walls exposed to fire, Numer. Heat Tran., Part A: Applications 29 (4) (1996) 373–395, https://doi.org/10.1080/10407789608913798. ISSN 1040-7782, http://www.tandfonline.com/doi/abs/10.1080/10407789608913798.

[8] D. Gawin, C. Majorana, B. Schrefler, Numerical analysis of hygro-thermal behaviour and damage of concrete at high temperature, Mechanics of Cohesive-frictional Materials, Int. J. Exp. Modell. Comput. Mater. Struct. 4 (1) (1999) 37–74.

[9] D. Gawin, F. Pesavento, B.A. Schrefler, Modelling of hygro-thermal behaviour of concrete at high temperature with thermo-chemical and mechanical material degradation, Comput. Methods Appl. Mech. Eng. 192 (13–14) (2003) 1731–1771, https://doi.org/10.1016/S0045-7825(03)00200-7. ISSN 00457825.

[10] K. Hertz, Concrete strength for fire safety design, Mag. Concr. Res. 57 (2005) 445–453, https://doi.org/10.1680/macr.2005.57.8.445.

[11] A. Millard, P. Pimienta, Modelling of Concrete Behaviour at High Temperature. State-Of-The-Art Report of the RILEM Technical Committee 227-HPB, Springer, 2019.

[12] A.V. Luikov, Heat and mass transfer in capillary-porous bodies, in: Advances in Heat Transfer, 1, Elsevier, 1964, pp. 123–184.

[13] Z.P. Bažant, Analysis of pore pressure, thermal stress and fracture in rapidly heated concrete, in: Proceedings International Workshop on Fire Performance of High-Strength Concrete, vol. 5, National Institute of Standards and Technology, 1997, pp. 155–164.

[14] Z.P. Bažant, M. Jirásek, Creep and Hygrothermal Effects in Concrete Structures, 225, Springer, Dordrecht, The Netherlands, 2018, https://doi.org/10.1007/978-94-024-1138-6, 9789402411362.

[15] D. Gawin, F. Pesavento, B.A. Schrefler, What physical phenomena can be neglected when modelling concrete at high temperature? A comparative study. Part 2: comparison between models, Int. J. Solid Struct. 48 (13) (2011) 1945–1961, https://doi.org/10.1016/j.ijsolstr.2011.03.003. ISSN 00207683.

[16] ISSN 0737-3937 Z.X. Gong, B. Song, A.S. Mujumdar, Numerical simulation of drying of refractory concrete, Dry. Technol. 9 (2) (1991) 479–500, https://doi.org/10.1080/07373939108916677, http://www.tandfonline.com/doi/abs/10.1080/07373939108916677.

[17] Z.X. Gong, A.S. Mujumdar, The influence of an impermeable surface on pore steam pressure during drying of refractory concrete slabs, Int. J. Heat Mass Tran. 38 (7) (1995) 1297–1303, https://doi.org/10.1016/0017-9310(94)00239-R, 00179310.

[18] G. Palmer, J. Cobos, J. Millard, T. Howes, The accelerated drying of refractory concrete - Part 2 numerical modelling, Refractories Worldforum 6 (4) (2014) 89–97.

[19] M.H. Moreira, R.F. Ausas, S. Dal Pont, P.I. Pelissari, A.P. Luz, V.C. Pandolfelli, Towards a single-phase mixed formulation of refractory castables and structural concrete at high temperatures, Int. J. Heat Mass Tran. 171 (2021), https://doi.org/10.1016/j.ijheatmasstransfer.2021.121064.

[20] D. Gawin, F. Pesavento, B.A. Schrefler, What physical phenomena can be neglected when modelling concrete at high temperature? A comparative study. Part 1: physical phenomena and mathematical model, Int. J. Solid Struct. 48 (13) (2011) 1945–1961, https://doi.org/10.1016/j.ijsolstr.2011.03.004. ISSN 00207683.

[21] ISSN 1359-5997 D. Gawin, F. Pesavento, B.A. Schrefler, Modelling of deformations of high strength concrete at elevated temperatures, Mater. Struct. 37 (4) (2004) 218–236, https://doi.org/10.1007/BF02480631,

WARNING!!! TEXT MISMATCH WITH THE INTERREF. PLEASE CHECK

https://www.rilem.net/boutique/fiche.php?cat=journal {&}reference=1578{%} 5Cn, http://www.springerlink.com/index/10.1007/BF02480631.
[22] T. Zhou, K. Ioannidou, F.-J. Ulm, M.Z. Bazant, R.-M. Pellenq, Multiscale poromechanics of wet cement paste, Proc. Natl. Acad. Sci. Unit. States Am. 116 (22) (2019) 10652–10657.
[23] K.G. Fey, I. Riehl, R. Wulf, U. Gross, Experimental and numerical investigation of the first heat-up of refractory concrete, Int. J. Therm. Sci. 100 (125) (2016) 108, https://doi.org/10.1016/j.ijthermalsci.2015.09.010. ISSN 12900729.
[24] F. Pesavento, M. Pachera, B. Schrefler, D. Gawin, A. Witek, Coupled numerical simulation of fire in tunnel, in: AIP Conference Proceedings, vol. 1922, AIP Publishing LLC, 2018, 090003.
[25] K. Bergmeister, P. Brunello, M. Pachera, F. Pesavento, B.A. Schrefler, Simulation of fire and structural response in the Brenner Base Tunnel by means of a combined approach: a case study, Eng. Struct. 211 (2020) 110319.
[26] K.G. Fey, I. Riehl, R. Wulf, U. Gross, Pressure driven heat-up curves– A numerical and experimental investigation, Int. J. Therm. Sci. 113 (1–9) (2017), https://doi.org/10.1016/j.ijthermalsci.2016.09.013. ISSN 12900729.
[27] ISSN 12900729 K.-G. Fey, I. Riehl, R. Wulf, U. Gross, First heat-up of 1D multi-layer walls and 2D geometries consisting of refractory concrete, Int. J. Therm. Sci. 116 (2017) 159–171, https://doi.org/10.1016/j.ijthermalsci.2016.11.021, http://linkinghub.elsevier.com/retrieve/pii/S1290072915302726.
[28] R.T. Tenchev, L. Li, J. Purkiss, Finite element analysis of coupled heat and moisture transfer in concrete subjected to fire, Numer. Heat Tran. Part A: Applications 39 (7) (2001) 685–710.
[29] ISSN 1040-7782 C.T. Davie, C.J. Pearce, N. Bićanić, Coupled heat and moisture transport in concrete at elevated temperatures — effects of capillary pressure and adsorbed water, Numer. Heat Tran., Part A: Applications 49 (8) (2006) 733–763, https://doi.org/10.1080/10407780500503854, http://www.tandfonline.com/doi/abs/10.1080/10407780500503854.
[30] P. Kalifa, F.-D. Menneteau, D. Quenard, Spalling and pore pressure in HPC at high temperatures, Cement Concr. Res. 30 (12) (2000) 1915–1927.
[31] D. Dauti, A. Tengattini, S. Dal Pont, N. Toropovs, M. Briffaut, B. Weber, Analysis of moisture migration in concrete at high temperature through in-situ neutron tomography, Cement Concr. Res. 111 (2018) 41–55.
[32] D. Dauti, S. Dal Pont, M. Briffaut, B. Weber, Modeling of 3D moisture distribution in heated concrete: from continuum towards mesoscopic approach, Int. J. Heat Mass Tran. 134 (2019) 1137–1152.
[33] D. Dauti, A. Tengattini, S. Dal Pont, N. Toropovs, M. Briffaut, B. Weber, Some Observations on Testing Conditions of High-Temperature Experiments on Concrete: an Insight from Neutron Tomography, Transport in Porous Media, 2020, pp. 1–12.
[34] M. S. Alnæs, J. Blechta, J. Hake, A. Johansson, B. Kehlet, A. Logg, C. Richardson, J. Ring, M. E. Rognes, G. N. Wells, "The FEniCS Project version 1.5", Archiv. Numerical Software 3 (100), doi:10.11588/ans.2015.100.20553.
[35] C.T. Davie, C.J. Pearce, N. Bićanić, A fully generalised, coupled, multi-phase, hygro-thermo-mechanical model for concrete, Mater. Struct. 43 (1) (2010) 13–33.
[36] L. Stelzner, B. Powierza, T. Oesch, R. Dlugosch, F. Weise, Thermally-induced moisture transport in high-performance concrete studied by X-ray-CT and 1 H-NMR, Construct. Build. Mater. 224 (2019) 600–609, https://doi.org/10.1016/j.conbuildmat.2019.07.065. ISSN 0950-0618.
[37] B. Powierza, L. Stelzner, T. Oesch, C. Gollwitzer, F. Weise, G. Bruno, Water migration in one-side heated concrete: 4D in-situ CT monitoring of the moisture-clog-effect, J. Nondestr. Eval. 38 (1), ISSN 15734862, doi:10.1007/s10921-018-0552-7.
[38] A. Tengattini, N. Lenoir, E. Andò, B. Giroud, D. Atkins, J. Beaucour, G. Viggiani, NeXT-grenoble, the neutron and X-ray tomograph in grenoble, in: Nuclear Instruments and Methods in Physics Research Section A: Accelerators, Spectrometers, Detectors and Associated Equipment, 2020, p. 163939.
[39] J.N. Reddy, An Introduction to the Finite Element Method, vol. 2, McGraw-hill, New York, 1993.
[40] D. Gawin, F. Pesavento, B.A. Schrefler, Comments to the paper "An application of a damage constitutive model to concrete at high temperature and prediction of spalling" by Rosen Tenchev and Phil Purnell [Int. J. Solids Struct. 42 (26)(2005) 6550–6565], Int. J. Solid Struct. 44 (11–12) (2007) 4234–4237.
[41] R. Tenchev, P. Purnell, Reply to comments to the paper "An application of a damage constitutive model to concrete at high temperature and prediction of spalling" by Rosen Tenchev and Phil Purnell [Int. J. Solids Struct. 42 (26)(2005) 6550–6565], Int. J. Solid Struct. 44 (11–12) (2007) 4238–4241.
[42] S. Dal Pont, F. Meftah, B. Schrefler, Modeling concrete under severe conditions as a multiphase material, Nucl. Eng. Des. 241 (3) (2011) 562–572.
[43] D. Dauti, A combined experimental and numerical approach to spalling of high-performance con crete due to fire, Theses, Université Grenoble Alpes, 2018, https://tel.archives-ouvertes.fr/tel-01950731.
[44] B. Weber, D. Dauti, S. Dal Pont, COMSOL Implementation of a porous media model for simulating pressure development in heated concrete, in: Comsol Conference, 2016.
[45] B.A. Schrefler, C.E. Majorana, G.A. Khoury, D. Gawin, Thermo-hydro-mechanical modelling of high performance concrete at high temperatures, Eng. Comput. 19 (7) (2002) 787–819.
[46] M.A. Al Fadul, K.R. Mackie, Numerical analysis of coupled heat and mass transfer phenomena in concrete at elevated temperatures, Transport Porous Media 122 (2) (2018) 437–458.
[47] A. Tengattini, S. Dal Pont, H. Cheikh Sleiman, F. Kisuka, M. Briffaut, Quantification of evolving moisture profiles in concrete samples subjected to temperature gradient by means of rapid neutron tomography: influence of boundary conditions, hygro-thermal loading history and spalling mitigation additives, Strain 56 (6) (2020), e12371.